Graphical Abstract

A Generalized Reduced Fluid Dynamic Model for Flow Fields and Electrodes in Redox Flow Batteries

Ziqiang Cheng[=], Kevin M. Tenny[=], Alberto Pizzolato, Antoni Forner-Cuenca, Vittorio Verda, Yet-Ming Chiang, Fikile R. Brushett, Reza Behrou

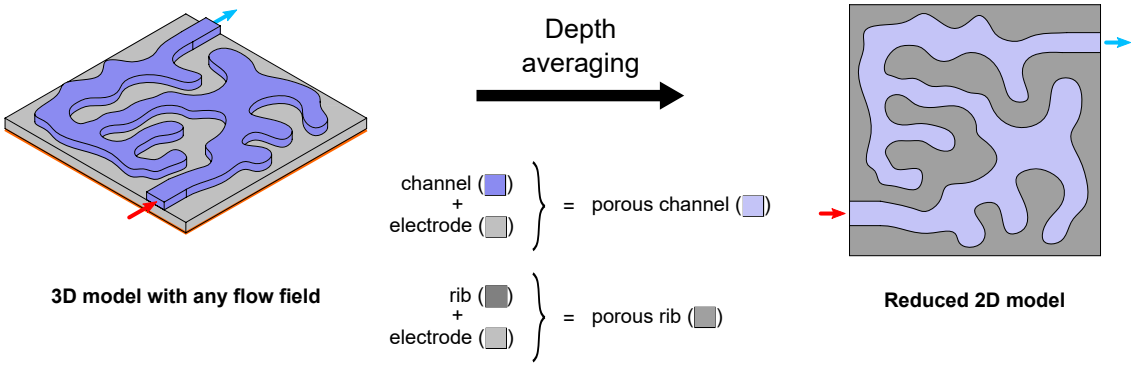

A Generalized Reduced Fluid Dynamic Model for Flow Fields and Electrodes in Redox Flow Batteries

Ziqiang Cheng[=a], Kevin M. Tenny[=b,c], Alberto Pizzolato[a], Antoni Forner-Cuenca[d], Vittorio Verda[a], Yet-Ming Chiang[b,e], Fikile R. Brushett[b,c,*], Reza Behrou[f,*]

[a]*Department of Energy, Politecnico di Torino, Turin, Italy*
[b]*Joint Center for Energy Storage Research, Massachusetts Institute of Technology, Cambridge, MA, USA*
[c]*Department of Chemical Engineering, Massachusetts Institute of Technology, Cambridge, MA, USA*
[d]*Department of Chemical Engineering and Chemistry, Eindhoven University of Technology, Eindhoven, The Netherlands*
[e]*Department of Materials Science and Engineering, Massachusetts Institute of Technology, Cambridge, MA, USA*
[f]*Department of Mechanical and Aerospace Engineering, University of California San Diego, La Jolla, CA, USA*

Abstract

High dimensional models typically require a large computational overhead for multiphysics applications, which hamper their use for broad-sweeping domain interrogation. Herein, we develop a modeling framework to capture the through-plane fluid dynamic response of electrodes and flow fields in a redox flow cell, generating a computationally inexpensive two-dimensional (2D) model. We leverage a depth averaging approach that also accounts for variations in out-of-plane fluid motion and departures from Darcy's law that arise from averaging across three-dimensions (3D). Our Resulting depth-averaged 2D model successfully predict the fluid dynamic response of arbitrary in-plane flow field geometries, with discrepancies of $< 5\,\%$ for both maximum velocity and pressure drop. This corresponds to reduced computational expense, as compared to 3D representations ($<$ 1% of duration and 10% of RAM usage), providing a platform to screen and optimize a diverse set of cell geometries.

Keywords: Redox flow batteries, Numerical modeling, Depth averaging, Flow Field, Electrode, Fluid dynamics

*Corresponding authors:
Email addresses: brushett@mit.edu (Fikile R. Brushett), rbehrou@eng.ucsd.edu (Reza Behrou)

Nomenclature

List of symbols

$\mathfrak{s}$	total perimeter of Ω_{pr} [m]
$\mathfrak{s}'$	length of the $\Omega_{pc} - \Omega_{pr}$ interfaces [m]
$\tilde{x}$	non-dimensional spatial parameter ranging from 0 to 1 [–]
H	thickness [m]
K_1	non-dimensional parameter in estimating λ_{opt} [–]
K_2	non-dimensional parameter in estimating λ_{opt} [–]
L	electrode or channel length [m]
Q	volumetric flow rate [$\mathrm{m^3\,s^{-1}}$]
w	width [m]
Δp	pressure drop [Pa]
$\overline{p}$	depth-averaged pressure [Pa]
$\overline{u}$	depth-averaged velocity [m]
i	3D index ($i \in \{x, y, z\}$) [–]
j	3D index ($j \in \{x, y, z\}$) [–]
k	2D index ($k \in \{x, y\}$) [–]
l	2D index ($l \in \{x, y\}$) [–]
N	number of channels [–]
n	outward unit normal vector [–]
p	pressure [Pa]
x	coordinate in channel length direction [m]
y	coordinate in channel width direction [m]
z	coordinate in half-cell thickness direction [m]

u	velocity [$\mathrm{m\,s^{-1}}$]

Greek symbols

Γ	boundaries [–]
κ	permeability [$\mathrm{m^2}$]
λ	pressure gradient corrector [–]
Ω	computational domains [–]
$\overline{\kappa}$	equivalent permeability [$\mathrm{m^2}$]
$\overline{\varepsilon}$	equivalent porosity [$\mathrm{m^2}$]
μ	viscosity [$\mathrm{Pa\,s}$]
ρ	density [$\mathrm{kg\,m^{-3}}$]
ε	porosity [–]

Subscripts

ch	channels
eq	equivalent quantity
e	electrode
in	inlet
opt	optimal
out	outlet
pc	porous-channel
pr	porous-rib
rib	rib
tot	electrode and flow field (rib or channel)
ref	reference quantity

Abbreviations

IDFF	Interdigitated flow field

PFF	Parallel flow field
RAM	Random-access memory
RFB	Redox flow battery
SFF	Serpentine flow field
VRFB	Vanadium redox flow battery

1. Introduction

Despite distinct advantages over the other battery systems, broad commercialization of redox flow batteries (RFBs) has been hampered by technical challenges, such as polarization losses that lower the power density, as well as appreciably pumping work that limits the energy efficiency [1–4]. To mitigate these issues, significant efforts have been made to bolster performance without increasing cost, such as leveraging alternative redox couples with fast kinetics [5], improving electrode morphologies to unlock higher surface area and enhanced mass-transport properties [1], and identifying new membranes for higher selectivity [6, 7]. Among these efforts, flow field engineering can be an effective and potentially more accessible approach, realizable by altering geometries [8] without modifications at the material level.

As one of the several key RFB components, the flow field serves multiple major functions [9, 10], including, but not limited to: (*i*) offering mechanical support of the electrodes, (*ii*) providing a low-resistance path for the electric current, and (*iii*) uniformly distributing the reactants over electrode to reduce the mass transport polarization. However, conventional flow field designs originate from PEMFC and are optimized for physical domains aberrant to that of RFBs [11]. As such, there have been various modeling pursuits to improve flow field architectures, but these computational thrusts are hindered by the highly non-linear fluid dynamic relationships that manifest in high-dimensional models [11, 12]. Consequently, while various three-dimensional (3D) models exist for RFB [8, 9, 12–21], high-throughput screening of diverse, multidimensional structures can be intractable. For example, the necessity for large computer resources (e.g., memory, power supply, etc.) limits the scalability of the 3D models to millimeters [20, 21], reducing their efficacy in full-scale applications [12, 22]. All of these motivate reduced models that retain fluid dynamic information for both the

flow field and the porous electrode.

Reduced models are an attractive as, if appropriately posed, they accurately capture high-dimensional functionalities with drastically smaller computational overhead. Indeed, various research efforts have generated low-order models for multiphysics simulations [11, 23–27], enabling rapid processing of highly non-linear physical domains. For example, Behrou et al. recently generated a two-dimensional (2D) model that successfully predicts the fluid dynamic and electrochemical performance in the through-plane direction of PEMFCs [28]. Consequently, designs like the serpentine and parallel flow fields were modeled in 2D at a fraction of the computational resources, as compared to in-plane models [27]. The resulting model employed depth-averaging, which averages along a spatial direction to reduce computational complexity, and was accurate across various flow field rib and channel geometries. This model was later incorporated into topological optimization algorithms, engendering new structures for improved PEMFC operation. Despite success in predicting the PEMFC fluid dynamic and electrochemical behaviors for traditional flow field designs, direct use of depth-averaging in RFB models results in large pressure drop discrepancies when compared to the 3D model predictions. We posit the inaccuracies of the depth-averaged model are due to the neglected pressure loss contributions from in-plane and out-of-plane motions in porous electrode portion under the channels. This motivated us to revisit the equations and derivations reported by Behrou et al. [28] to generate an extended modeling framework, which we then apply to the fluid dynamics of a redox flow cell.

Herein, we describe the formulation of a depth-averaged model for RFB flow fields and electrodes, where we derive a system of equations for two domains, the electrode / flow field channel and the electrode / flow field rib that, when combined, create one-half of the RFB cell. We then compare these equations with 3D simulations to identify a correction parameter for out-of-plane pressure loss that we subsequently scrutinize across a range of flow field geometries. We conclude by demonstrating the computational lightness of our depth-averaged model and highlight areas to improve the model for follow-up studies.

2. Physical Model

This section presents the numerical method to reduce the computationally-expensive 3D fluid dynamics problem to a 2D representation without sacrificing accuracy. The fluid dynamic operating equations are similar across RFB chemistries; however, for this work we elect to use a vanadium

redox flow cell as an example. A comprehensive detail on the 3D model (e.g., governing equations and model parameters) can be found in Cheng et al. [27]. Unless otherwise stated, we omit the detailed formulation of the governing equations and model parameters, which are provided in the Supporting Information. Additionally, along with the assumptions previously reported for the 3D model [27], we hypothesize that the flow field depth is constant for all numerical examples presented in this work.

2.1. Depth-averaging scheme

Typical numerical depth-averaging schemes neglect variations of flow and transport properties across at least one spatial direction and have been employed for modeling of fluid flow over a range of length scales [29–33]. The application of the depth-averaging scheme for multiphysics energy storage and conversion systems, such as fuel cells or RFBs, is less well studied and remains an active area of research [28] Behrou et al. applied the depth-averaging scheme on modeling and design optimization of gas flow channels in PEMFCs [28]. However, a direct use of their depth-averaging approach in RFB model yields a large discrepancy in pressure drop compared to the 3D model predictions, as discussed in Section S1 of the Supporting Information. Here, we revisit the depth-averaging approach presented in Behrou et al. and address the pressure discrepancy with a generalized numerical framework, which is subsequently used to contemplate a diverse array of flow field geometries for RFB cells [28].

As reported in Behrou et al. and shown as Fig. 1, a 2D depth-averaging plane consisting of porous-channel (Ω_{pc}) and porous-rib (Ω_{pr}) regions is chosen as the 2D computational domain to account for the simultaneous effects of flow field geometry and the under-rib flow [28]. The equivalent bulk properties (i.e., porosity, ε, and permeability, κ) for porous-channel and porous-rib regions are approximated as follows:

$$\overline{(\cdot)} = \begin{cases} \dfrac{(\cdot)_e H_e + (\cdot)_{ch} H_{ch}}{H_e + H_{ch}}, & \text{in } \Omega_{pc} \\ \\ \dfrac{(\cdot)_e H_e + (\cdot)_{rib} H_{ch}}{H_e + H_{ch}}, & \text{in } \Omega_{pr} \end{cases} \tag{1}$$

where $\overline{(\cdot)}$ is the depth-averaged quantity and $(\cdot)$ indicates a generic bulk property and H is the thickness, with subscript e, ch, and rib referring to electrode, channel, and rib, respectively.

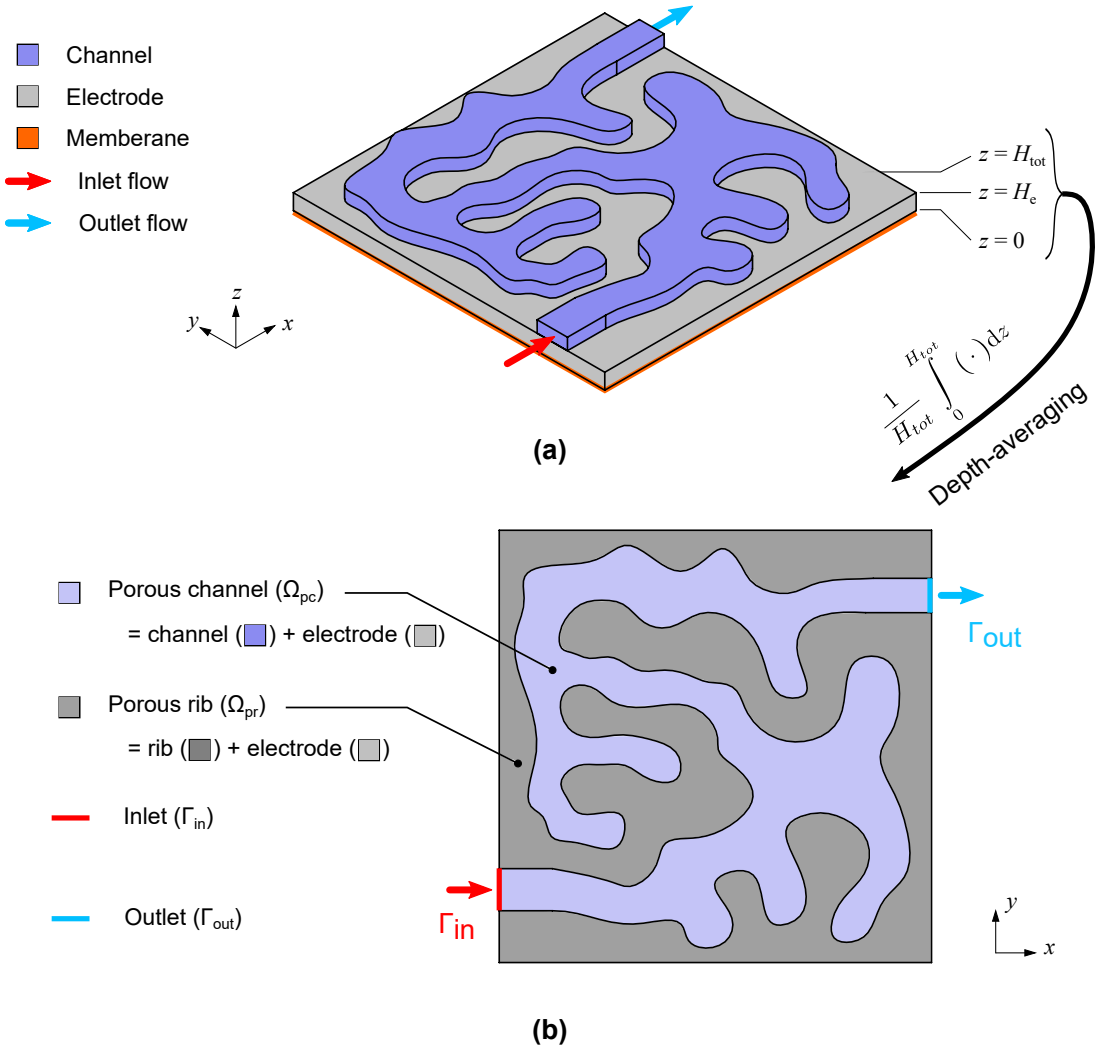

Figure 1: Schematic representations of: (a) a half-cell including membrane, electrode, and channels of flow field, and (b) a planar computational domain reduced from (a) via depth-averaging, aimed to characterize the half-cell fluid dynamic behavior for any arbitrary flow field geometry. H_{tot} is the sum of H_e and H_{ch}, which are thickness of electrode and flow field, respectively.

2.2. Governing equations

As shown in Fig. 1, the 3D fluid dynamic state variables (i.e., the velocity vector, u_i, and the pressure, p, with $i \in \{x, y, z\}$) are reduced to planar quantities through depth-averaging process as

follows:

$$\overline{(\cdot)} = \frac{1}{H_e + H_{ch}} \int_0^{H_e+H_{ch}} (\cdot)\, \mathrm{d}z, \tag{2}$$

where $(\cdot)$ refers to a generic 3D state variable and $\overline{(\cdot)}$ is the corresponding depth-averaged value that is henceforth adopted. In addition, for convenience, we define an overall thickness as $H_{tot} = H_e + H_{ch}$. For brevity, only important findings and conclusions present in this work, and the comprehensive details can be found in the Supporting Information.

2.2.1. Conservation of mass

The 3D continuity equation can be depth-averaged due to the non-slip boundary conditions at both ends (i.e., $z = 0$ and $z = H_e + H_{ch}$ in Ω_{pc}, and $z = 0$ and H_e in Ω_{pr}) and the constant depth assumption, where the depth of channel and electrode is assumed to stay constant [31]:

$$\frac{\partial \overline{u}_k}{\partial x_k} = 0 \quad \text{in } \Omega_{pr} \cup \Omega_{pc}, \tag{3}$$

where k stands for the planar index ($k \in \{x, y\}$), differentiating from the 3D index i or j ($i, j \in \{x, y, z\}$). The details of the relevant derivations can be found in the Section S2.1 of the Supporting Information.

2.2.2. Conservation of momentum in Ω_{pc}

The 3D momentum equation consists of the incompressible Navier-Stokes equation in the free flow channel and Brinkman equation in the porous electrode, both of which are highly non-linear. Therefore, we introduce approximations to simplify the depth averaging procedure. Specifically, we assume (i) the viscous effects dominate such that inertia terms on the pressure gradient are negligible; (ii) the Brinkman equation governing the fluid dynamic behavior in the electrode [27] is assumed to be interchangeable with Darcy's law [34]; and, (iii) the flow pattern in channel can be approximated as Poiseuille flow [35]. These assumptions are further investigated and justified through additional studies in Section S2.2 of the Supporting Information.

Consequently, the 2D momentum conservation equation deviates from the one reported in Behrou et al. [28]. We derive the 2D momentum conservation equation by depth-averaging of the 3D version as follows:

$$\frac{\rho}{\overline{\varepsilon}^2} \overline{u}_l \frac{\partial \overline{u}_k}{\partial x_l} = -\frac{\partial \overline{p}}{\partial x_k} + \frac{\mu}{\overline{\varepsilon}} \frac{\partial}{\partial x_l} \frac{\partial \overline{u}_k}{\partial x_l} - \frac{12\mu}{H_{ch}^2} \overline{u}_k + \frac{H_e}{H_{tot}} \frac{\partial \overline{p}}{\partial x_k} \quad \text{in } \Omega_{pc}, \tag{4}$$

where l represents another 2D index distinct from k, μ is the electrolyte viscosity, ρ is the electrolyte density, and $\overline{\varepsilon}$ refers to the depth-averaged porosity, defined in Eq. (1). Compared to the reported momentum equation in Behrou et al. [28], Eq. (4) has an additional term, $H_e/H_{tot} \cdot \partial\overline{p}/\partial x_k$, derived from the Darcy term in the 3D Brinkman equation [27] over the electrode portion under the channels [36]. This term refers to in-plane pressure drop contribution due to in-plane motion in porous electrode portion under the channels [36]. In Behrou et al. [28], $-\mu/\overline{\kappa} \cdot \overline{u}_k$ is used instead [28], where $\overline{\kappa}$ is the corresponding depth-averaged permeability. However, $\overline{\kappa} = \infty$ in Ω_{pc}, according to its definition given in Eq. (1), meaning $-\mu/\overline{\kappa} \cdot \overline{u}_k$ is null in Ω_{pc}. Consequently, the pressure drop contribution due to in-plane motions under the porous electrode / channel portion is neglected in that work [28].

2.2.3. Conservation of momentum in Ω_{pr}

Following similar operations derived in Ω_{pc} (i.e., averaging the 3D governing equations along the z direction according to the defined planar state variables), the 3D conservation of momentum stated in Cheng et al. [27] can be depth-averaged as

$$\frac{\rho}{\overline{\varepsilon}^2}\overline{u}_l\frac{\partial\overline{u}_k}{\partial x_l} = -\frac{\partial\overline{p}}{\partial x_k} + \frac{\mu}{\overline{\varepsilon}}\frac{\partial}{\partial x_l}\frac{\partial\overline{u}_k}{\partial x_l} - \frac{\mu}{\overline{\kappa}}\overline{u}_k \quad \text{in } \Omega_{pr}, \tag{5}$$

where $\overline{p}$ in Ω_{pr} is defined as follows:

$$\overline{p} = \frac{1}{H_e}\int_0^{H_e} p \, \mathrm{d}z \quad \text{in } \Omega_{pr}. \tag{6}$$

Unlike Eq. (2), the depth-averaged pressure equation (Eq. (6)) prevents a large jump at the Ω_{pc}-Ω_{pr} interfaces. Details on the derivations and verification can be found in Section S2.3 of the Supporting Information.

Eqs. (3)–(5) are still unable to provide an acceptable fluid dynamic prediction for the 2D half cell model because an important flow behavior is absent from the derived momentum equations (i.e., Eqs. (4) and (5)). This mismatch is related to the pressure discontinuity at the Ω_{pc}-Ω_{pr} interfaces, which can be captured with the 3D model, revealing the limitations of the 2D formulation.

As an example, we use the 3D simulation with interdigitated flow field (IDFF) presented in Cheng et al. [27] to illustrate the existence of this pressure discontinuity at the Ω_{pc}-Ω_{pr} interfaces and its impact on the 2D model. The distribution of depth-averaged 3D pressure (i.e., $\overline{p}$, defined as Eq. (2) in Ω_{pc} and Eq. (6) in Ω_{pr}) along a y-directed line with $x = 0$ is shown in Fig. 2a. The

results clearly demonstrate this discontinuity at the Ω_{pc}-Ω_{pr} interface. Furthermore, comparison of the y-directed depth-averaged 3D pressure distribution with the corresponding 2D version, as depicted in Fig. 2a, shows that the 2D model cannot capture this discontinuity, thus leading to a significant pressure discrepancy.

To investigate this discontinuity, the 3D pressure distribution along two y-directed lines at $x = 0$ across half channel ($z = H_e + H_{ch}/2$) and half electrode ($z = H_e/2$) are compared with the corresponding depth-averaged 3D pressure at the same x location (Fig. 2b). The discontinuity stems from the out-of-plane pressure losses, due to out-of-plane fluid motion (Fig. 3). To address this issue with minimal complexity, we introduce a dimensionless correction factor, λ, to adjust the pressure gradient in Ω_{pr} of the 2D model. As illustrated in Fig. 2c, the correction factor in Ω_{pr} is defined as:

$$\lambda = \frac{\left.\frac{\partial \overline{p}}{\partial x_k}\right|_{\text{uncorrected}}}{\left.\frac{\partial \overline{p}}{\partial x_k}\right|_{\text{corrected}}} \quad \text{in } \Omega_{pr}, \tag{7}$$

where $\partial\overline{p}/\partial x_k|_{\text{uncorrected}}$ is the pressure gradient defined in Eq. (5). Hence, the uncorrected pressure gradient term in Eq. (5) can be replaced by $\lambda\, \partial\overline{p}/\partial x_k|_{\text{corrected}}$ as follows:

$$\frac{\rho}{(\lambda\overline{\varepsilon})^2}\overline{u}_l\frac{\partial \overline{u}_k}{\partial x_l} = -\frac{\partial \overline{p}}{\partial x_k} + \frac{\mu}{\lambda\overline{\varepsilon}}\frac{\partial}{\partial x_l}\frac{\partial \overline{u}_k}{\partial x_l} - \frac{\mu}{\lambda\overline{\kappa}}\overline{u}_k \quad \text{in } \Omega_{pr}. \tag{8}$$

Additional details on the derivation can be found in Section S2.3 of the Supporting Information. For simplicity, the subscript "corrected" is eliminated from Eq. (8). The optimal value of the pressure gradient correction factor also varies with respect to the rib width and the electrode thickness as:

$$\lambda_{opt} = \frac{K_1}{\frac{H_e}{w_{rib}} + K_2}, \tag{9}$$

where K_1 and K_2 are scalar constants close to 1 and with a weak dependency on H_e, hence Eq. (9) can be approximated as:

$$\lambda_{opt} = \frac{1}{\frac{H_e}{w_{rib}} + 1}. \tag{10}$$

Moreover, further studies in this work demonstrate that Eq. (10) also holds for cases without a well-defined rib width if replacing w_{rib} in Eq. (10) with an equivalent rib widths ($w_{rib,eq}$) estimated as follows:

$$w_{rib,eq} \approx \frac{A_{rib}}{\mathfrak{s}/2}, \tag{11}$$

where A_{rib} and $\mathfrak{s}$ are the total area and perimeter of the porous rib region (Ω_{pr}), respectively. Further details on the derivation of Eqs. (9)–(11) are given in Section 2.4.

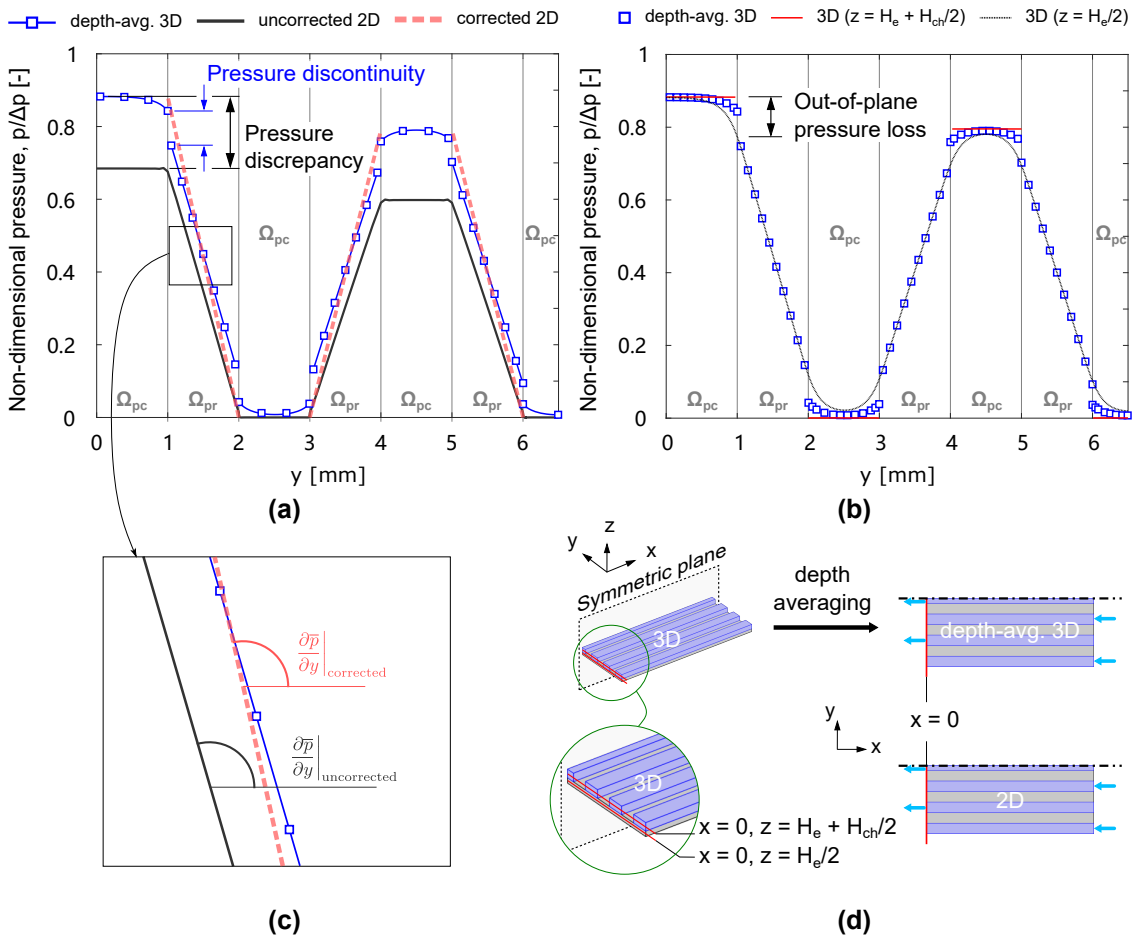

Figure 2: Comparison of pressure distribution along y direction for IDFF [27] at lines with same x location of $x = 0$ for different models including: (a) three lines for the depth-averaged 3D, uncorrected 2D, and corrected 2D models, respectively; (b) a line for the depth-averaged 3D model and two lines with different z locations ($z = H_e$ and $H_e + H_{ch}/2$) for the 3D model. In addition, (c) is a local enlargement of (a), and (d) is a schematic legend of the relevant $x = 0$ lines, including two of the 3D model ($z = H_e$ and $H_e + H_{ch}/2$), one of the depth-averaged 3D model, and one of the reduced 2D model. All data is obtained from simulations at Q_{ref} ($10\,\text{mL}\,\text{min}^{-1}$). Δp refers to the overall 3D pressure drop.

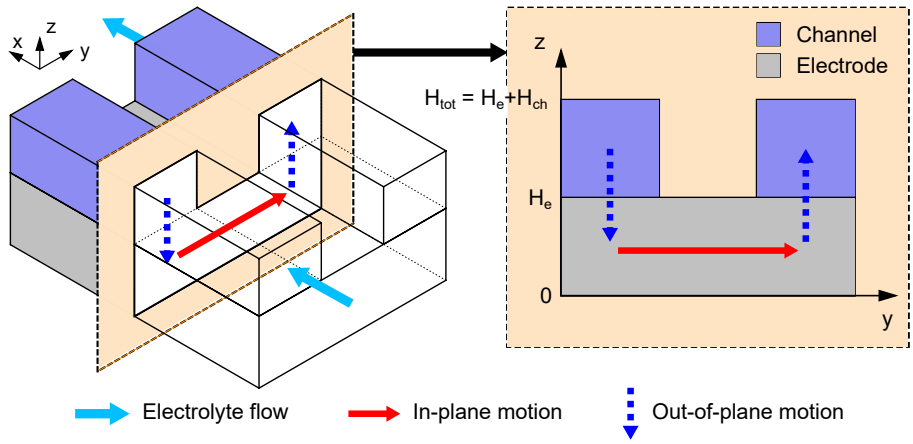

Figure 3: Schematic representation of the out-of-plane motion that causes out-of-plane pressure loss and thus leads to pressure continuity at the Ω_{pc}-Ω_{pr} interfaces.

2.3. Boundary conditions

Following Behrou et al. [28], at the inlet (Γ_{in}), the 3D fixed flow rate condition can be depth-averaged as:

$$-H_{tot} \cdot \int_{\Gamma_{in}} \overline{u}_k \, n_k \, \mathrm{d}s = Q \quad \text{at } \Gamma_{in}, \tag{12}$$

where Q is the volumetric flow rate and n_k is the outward unit normal vector. At the outlet (Γ_{out}), the pressure is greater than zero at the electrode portion ($0 \leq z \leq H_e$) of Γ_{out}. Therefore, an accurate depth-averaged pressure condition at the outlet is considered as follows:

$$\overline{p}_{out} = \frac{1}{H_{tot}} \left(\int_0^{H_e} p \, \mathrm{d}z + \int_{H_e}^{H_{tot}} p \, \mathrm{d}z \right) = \frac{1}{H_{tot}} \int_0^{H_e} p \, \mathrm{d}z \quad \text{at } \Gamma_{out}. \tag{13}$$

Eq. (13) is difficult to implement, given the pressure integration across the electrode is encompassed by the $z = 0$ to H_{tot} range of the 2D model. Therefore, an approximated version is employed:

$$\overline{p}_{out} = 0\,\mathrm{Pa} \quad \text{at } \Gamma_{out}. \tag{14}$$

This approximation also has good agreement when H_e is below a certain threshold; for example, $\overline{p}_{out}$ is smaller than 2 % of the overall 3D pressure drop if $H_e < 4H_{ch}$, as shown in Fig. 5c.

2.4. Pressure gradient correction factor λ in Ω_{pr}

This section presents the full details on Eqs. (9)–(11) above.

2.4.1. Parametric study of λ

We perform a parametric study to investigate the impact of flow fields and cell parameters on the behavior of λ. To generalize λ, we consider various flow field properties, such as the flow field type (e.g., IDFF, parallel flow field (PFF), and serpentine flow field (SFF)), the channel geometry, the channel and electrode thicknesses, and the channel and rib widths.

Impact of flow field types. We consider three distinct flow field types (IDFF, PFF, and SFF) as shown in Fig. 4a revealing that the optimal λ does not depend on flow field type, as all values converge to 0.73. The subsequent studies in this section show that convergence is dependent on their identical electrode thickness and rib width. Additionally, the IDFF possesses the greatest sensitivity to λ as compared to PFF and SFF, whereby IDFF has the highest percentage of flow rate penetrating into the porous media [37, 38]. Thus, we only consider the IDFF in the following parametric studies.

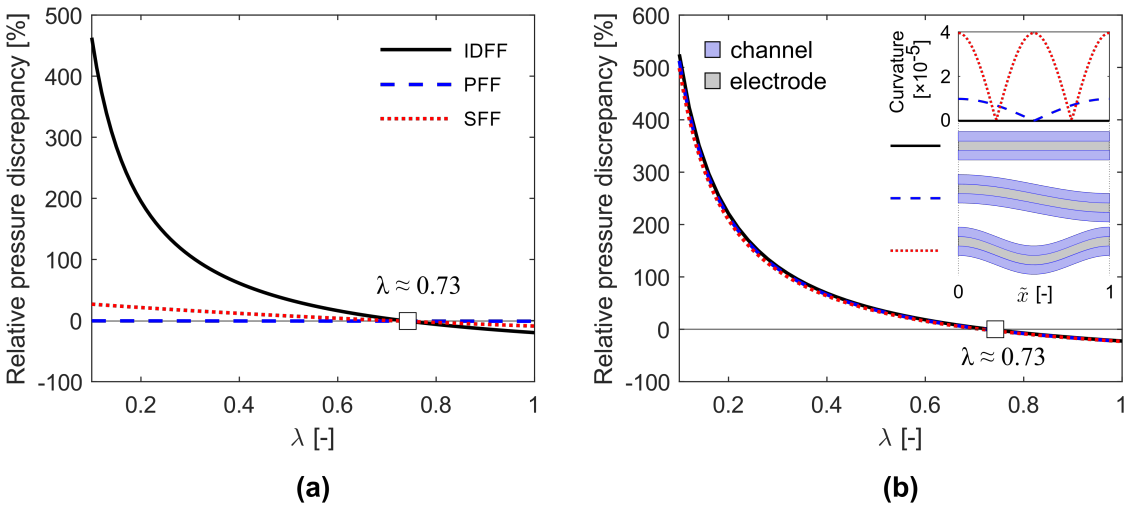

Figure 4: Variation of relative pressure discrepancies with respect to the value of λ from 0.1 to 1 for: (a) different flow field types, i.e., IDFF, PFF, and SFF, and (b) three IDFF geometries with different curvatures.

Impact of the channel curvature. Three different IDFF geometries with different curvatures are investigated. The first is straight channels with channel width of w_{ch}. The second and third are defined by $w_{ch}\cos(\pi\tilde{x})$ and $w_{ch}\cos(2\pi\tilde{x})$, respectively. The parameter $\tilde{x}$ is a dimensionless spatial parameter ranging from 0 to 1, corresponding to the left and right channel sides, respectively.

Therefore, the curvature can be analyzed in ascending order as first, second, and third, as shown in the legend of Fig. 4b, where the curvature distribution of three cases along channel length is calculated [39] and plotted. Similarly, all other geometrical parameters are fixed. The results shown in Fig. 4b suggest that the channel curvature does not affect the value of λ. Such independence can be explained as follows: the pressure gradient correction factor λ directly stems from the out-of-plane motions, which shows negligible correlation with the channel curvature. Furthermore, as the curvature mainly affects the configuration in the channel-length direction while the channel-width direction stays the same throughout $0 \leq \tilde{x} \leq 1$, the result suggests that factor that possibly impinges λ should be along the channel-width direction instead of the channel-length direction, if not considering the out-of-plane direction. Hence, we can use a straight IDFF to continue the study without considering the effect of channel curvature.

Impact of number of flow channels. A straight IDFF with five different number of channels (2, 4, 7, 9, and 11) is studied. The results given in Fig. S14a of Supporting Information reveal that the number of channels does not impact on the value of optimal λ. The arithmetic mean and standard deviation of the five obtained optimal λ values are 0.7310 and 0.0017, respectively. This result is as expected since changing the number of channels only alters the number of repeating units in the flow field and cannot affect the configuration inside the repeating unit. The critical influencing factor is expected to be within a repeating unit (e.g., two channels and an electrode portion in between them) of the flow field presented in the numerical experiments. To this end, for the rest of this study, all the following numerical experiments will be implemented on a straight, two-channel IDFF as depicted in Fig. S15 of Supporting Information. Unless otherwise stated, all the control variables are valued according to Cheng et al. [27].

Impact of the channel length and width. Similarly, as shown in Fig. S14b and c of Supporting Information, under a range channel lengths (L) and widths (w_{ch}), the arithmetic mean is ca. 0.73 with negligible standard deviations (e.g., 0.0003 for L and 0.0041 for w_{ch}, respectively). Therefore, it can be assumed that neither the channel length nor the channel width has significant effects on the optimal λ. The independence of the channel length is consistent with the analysis in channel curvature. Furthermore, the independence of the channel width suggests the rib width might be the influencing factor that affects value of λ, considering our analysis in channel curvature, i.e., the influencing factor should be along the channel-width direction.

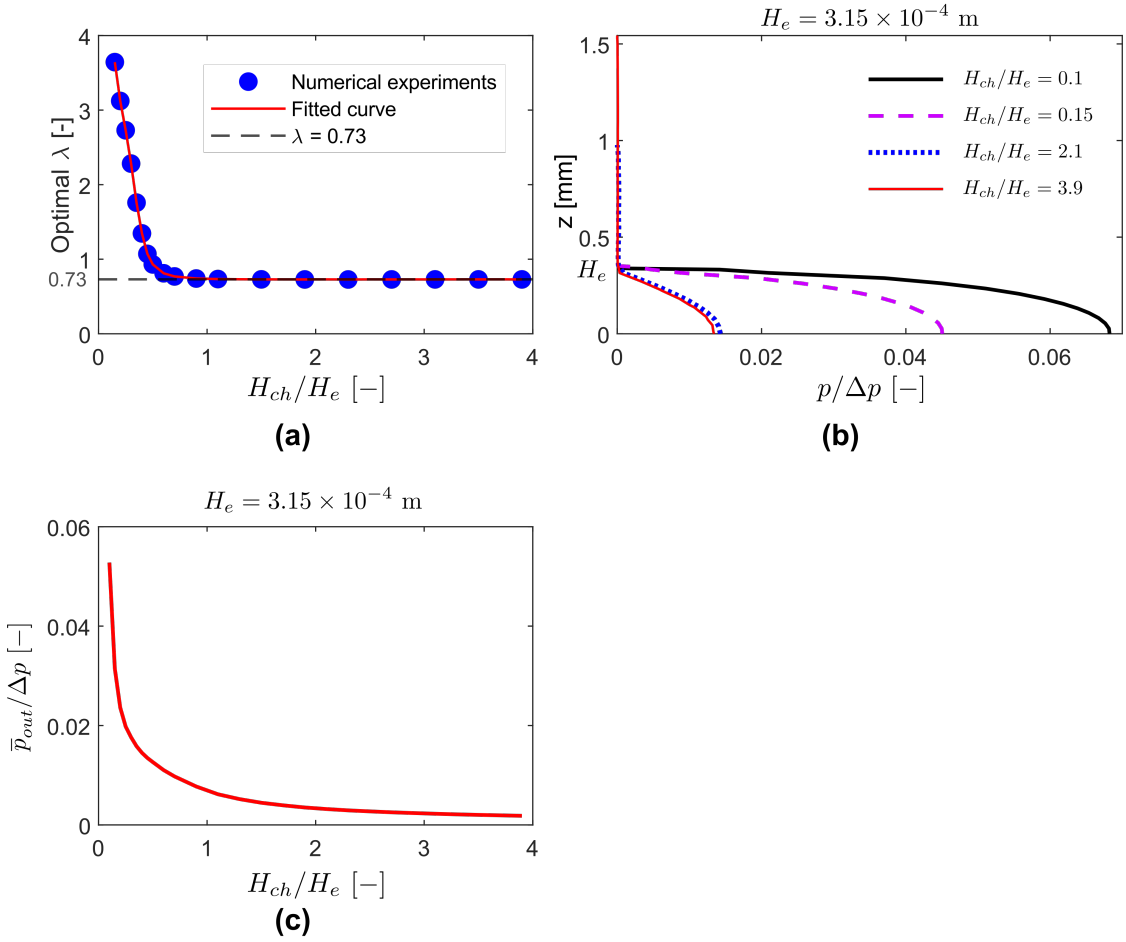

Figure 5: (a) Variation of the optimal λ with respect to different channel thickness; (b) pressure distribution along a z-directed centered line crossing outlet for different H_{ch}/H_e ratios; (c) variation of the non-dimensional depth-averaged outlet pressure with respect to H_{ch}/H_e ratio ranged from 0.1 to 3.9. Δp is the overall pressure drop.

Impact of the channel thickness. Further study on the channel thickness, as demonstrated in Fig. 5a, shows that the optimal λ is approximately constant with H_{ch} only when $H_{ch}/H_e \gtrapprox 0.5$. In the contrast, when $H_{ch}/H_e \lessapprox 0.5$, the optimal value of λ rises rapidly as H_{ch}/H_e decreases. As shown in Fig. 5b, the lower the channel thickness, the higher the depth-average pressure and the further away from the approximated outlet boundary condition (Eq. (14)). Additionally, the change in the overall pressure drop (i.e., $\overline{p}_{out}/\Delta p$) decreases with respect to H_{ch}/H_e (Fig. 5c). Therefore, it is reasonable to acknowledge that the rapid increase of the optimal λ during lower H_{ch}/H_e interval is

ascribed to the invalidity of the approximated outlet boundary condition (Eq. (14)). To this end, we can assume that the H_{ch}/H_e scope of the study will not beyond the lower non-constant region (i.e., $H_{ch}/H_e \lessapprox 0.5$), thus simplifying the problem and concluding that the optimal λ is not dependent on the channel thickness. This assumed range is widely consistent to experimental configurations reported in prior literature [9, 10, 37, 41–49]. For example, Xu et al. found an optimal electrode thickness of ca. 2/3 of channel thickness, which results in $H_{ch}/H_e \approx 1.5$ [43].

Impact of the rib width. A wide range of rib widths (w_{rib}) ranging from $0.01H_e$ to $0.98H_e$, where $H_e = 3.15 \times 10^{-4}$ m [27], is tested in our numerical experiments and reflects two pristine Freudenberg H23 electrodes (Fuel Cell Store) stacked and compressed by ca. 20%. Results shown in Fig. 6b reveal that the optimal λ presents a clear relationship with the ratio H_e/w_{rib} as follows:

$$\lambda_{opt} = \frac{0.98}{\frac{H_e}{w_{rib}} + 1.03}, \tag{15}$$

where the numbers 0.98 and 1.03 are obtained through the curve-fitting, implemented using the MATLAB®curve fitting toolbox [50].

Impact of the electrode thickness. Furthermore, similar numerical experiments for the trend of the optimal λ with respect to H_e/w_{rib} are repeated for various electrode thicknesses (Fig. 6). The range of H_e/w_{rib} between 0 and 1 is in good agreement with values extracted from related experimental configurations reported in previous literature [9, 10, 37, 41–46, 49, 51, 52]. A relationship between λ_{opt} and H_e/w_{rib} arises from these values, and we posit these are related through Eq. (9), where the scalar constants K_1 and K_2 increase with H_e. Indeed, the fitted trend is similar to Eq. (10) as long as the electrode thickness is greater than 1×10^{-4} m, as shown in Fig. 6a. This range ($H_e > 1 \times 10^{-4}$ m) is a common lower bound found in electrode offerings; for example, the minimum uncompressed thicknesses of five commercial electrodes has been previously reported as $(2.1 \pm 0.1) \times 10^{-4}$ m [53]. Overall, thicker electrodes increase the available active surface area and improve the performance; but when not limited by the active sites, the additional thickness leads to higher ohmic losses and hinders electrochemical performance [43].

2.4.2. Equivalent rib-width estimation

Despite the obtained relationship between λ_{opt}, H_e, and w_{rib}, there are still obstacles in generalizing a reduced planar model for arbitrary flow field geometries. Either Eq. (9) or Eq. (10) are

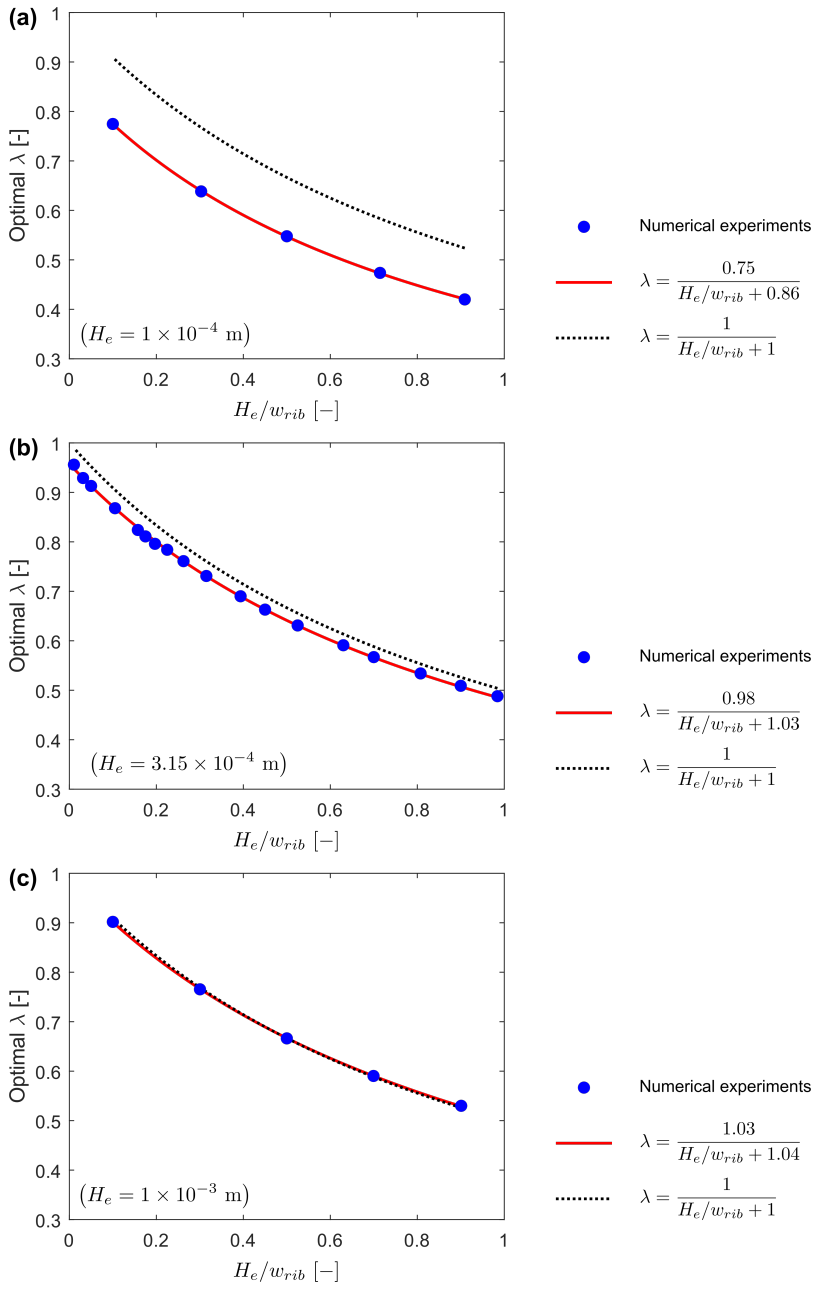

Figure 6: Variation of the optimal λ with respect to different rib width (w_{rib}), which is non-dimensionalized as ratio H_e/w_{rib}, for: (a) $H_e = 1 \times 10^{-4}$ m, (b) $H_e = 3.15 \times 10^{-4}$ m, and (c) $H_e = 1 \times 10^{-3}$ m.

obtained through a simplified straight, two-channel IDFF (Fig. S15 of Supporting Information), where the rib width is unique and well-defined. However, this may not always be the case, as evinced by the geometry reported in Ibrahimoglu et al. [54]. Hence, we present an approximated approach to estimate the equivalent rib width across arbitrary geometries.

As observed in Fig. 7, the average rib width for an IDFF-like geometry with N straight channels (with or without tapering) with well-defined channel length (L) can be approximated as follows:

$$w_{rib,eq} = \frac{A_{rib}}{NL}, \tag{16}$$

where A_{rib} is the total area of porous rib region. We note that Eq. (16) can be extended to a more

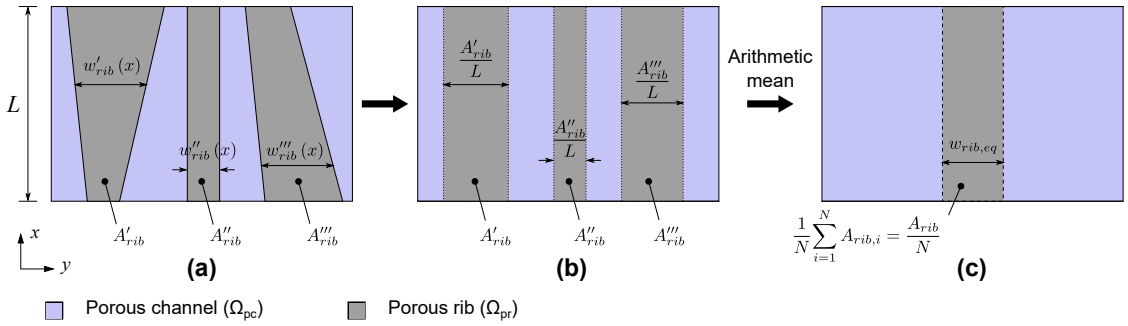

Figure 7: Schematic representations of the procedure to estimate the equivalent rib width (i.e., $w_{rib,eq}$) for an IDFF-like flow field with straight channels and well-defined channel length. $N = 3$ in this example.

generic, IDFF-like geometry without a clearly-defined L (e.g., Fig. 8a). Here, we take the advantage of the apparent positive correlation between NL and half of the length of the Ω_{pc}-Ω_{pr} interfaces, shown by $\mathfrak{s}'/2$. Hence, Eq. (16) can be approximated as:

$$w_{rib,eq} \approx \frac{A_{rib}}{\mathfrak{s}'/2}. \tag{17}$$

Further numerical studies show that replacing $\mathfrak{s}'$ with $\mathfrak{s}$, which refers to the total perimeter of the porous rib region (Ω_{pr}), gives better agreement especially for larger Ω_{pr} area (e.g., Fig. 8b), as it can be considered a pseudo-hydraulic diameter. Therefore, we conclude a more generalized estimation of the equivalent rib width as stated in Eq. (11).

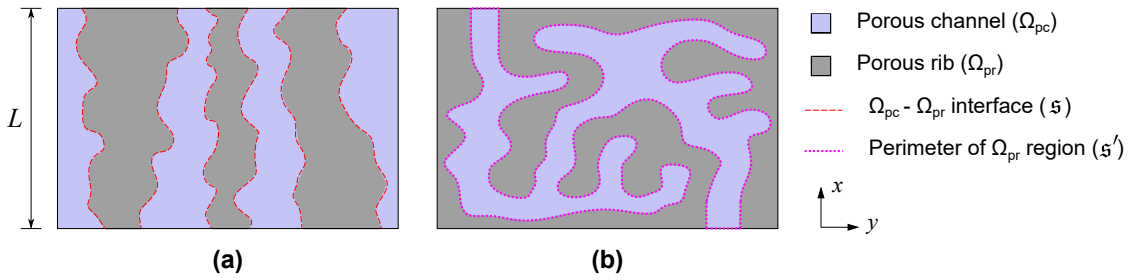

Figure 8: Schematic representations of: (a) a IDFF-like generic geometry with highlighted Ω_{pc}-Ω_{pr} interfaces to illustrate the positive correlation between $\mathfrak{s}/2$ and NL, and (b) a generic geometry with highlighted Ω_{pr} perimeter (i.e., $\mathfrak{s}'$) that will be used to estimate the equivalent rib width.

3. Model calibration and validation

3.1. Numerical solution

In this paper, we employ computational configurations similar to those reported in Cheng et al. [27], using COMSOL Multiphysics® [55]. The three-node triangle and four-node tetrahedral elements are used to discretize the 2D and 3D models, respectively. Mesh refinement studies are performed to ensure negligible discretization errors, with details on the mesh refinement studies given in Section S4 of the Supporting Information.

A machine with Intel® Core™ i5-8500 (Hexa-Core, 3.00 GHz) processor with a random-access memory (RAM) of 32 GB is used for all numerical simulations. Furthermore, the computational resource consumed for each p-Q point is compared between the 2D and 3D models (Table 1). As expected, the 2D models demand less than $< 1\,\%$ of the duration and $< 10\,\%$ of the RAM usage as compared to the corresponding 3D models. All other model and material parameters are adopted from Cheng et al. [27].

Table 1: Comparison of consumed computational resources averaged for each $p-Q$ point between 3D and 2D models (for the IDFF geometry).

Case	Memory usage	Average simulation duration
3D	29.2 GB	891.4 s / point
2D	2.1 GB	5.9 s / point

3.2. 2D model verification

In this section, we verify the reduced 2D model by considering a diverse range of flow field geometries. Apart from the aforementioned three classical straight-channel flow fields with well-defined rib widths (i.e., IDFF, PFF, and SFF) [27, 56], four different geometries artificially designed by the authors and three geometries described in previous literature [46, 54, 57] are simulated and carefully examined by comparing the fluid dynamic responses of the 2D and 3D models. All geometries have the same dimensions as the stated classical ones, whose geometric parameters can be found in the Supporting Information of Milshtein et al. [56]. Additionally, to examine the effectiveness of the approximated λ_{opt}, the corresponding results obtained from Eq. (10) are also included. For the brevity, only results from four representative cases are presented in this section, whereas the others are discussed in Section S5 of Supporting Information.

As depicted in the first and second sub-figures of each geometry in Fig. 9 (i.e., Fig. 9 a1 to d1 and a2 to d2), the corrected 2D models show good agreement in both the velocity and pressure fields, as compared to the full 3D domains at the reference flow rate of $10\,\mathrm{mL\,min^{-1}}$, regardless of how the λ is estimated. Further studies are performed by comparing the pressure drop prediction between the 2D and 3D models at different flow rates ranging from 0.1 to 1.5× of the reference flow rate [27, 28], which are presented in the third sub-figure of each case in Fig. 9. It can be observed that the 2D and 3D pressure drops closely match across all geometries within the low flow rate region, with the maximum relative discrepancy at $1\,\mathrm{mL\,min^{-1}}$ being 2.9 % and 4.2 % for λ_1 (estimated via Eq. (15)) and λ_2 (estimated via Eq. (10)), respectively. This agreement is a result of accounting for all significant physics that govern the desirable fluid dynamic phenomena, including the in-plane and out-of-plane motions in porous electrode portion of Ω_{pc}. The discrepancy for λ_1 can be ascribed to error in the estimation of the equivalent rib width, after comparison between the two groups presented in Fig. 9 — with and without a well-defined rib width. The former (Fig. 9a and b) results in a maximum discrepancy smaller than 0.5 % when using λ_1, whereas for the latter (Fig. 9c and d), the corresponding discrepancies are closer to 3 %. Furthermore, using λ_2 leads to additional $1 - 1.5$ % discrepancy with respect to λ_1 within the low flow rate region (e.g., at $1\,\mathrm{mL\,min^{-1}}$). Nevertheless, the results demonstrate that the 2D model can provide a reasonable pressure drop prediction with respect to the 3D simulations across a diverse range of flow field geometries, particularly in the low flow rate region.

However, deviations increase at elevated flow rates for certain geometries (i.e., Fig. 9b c and

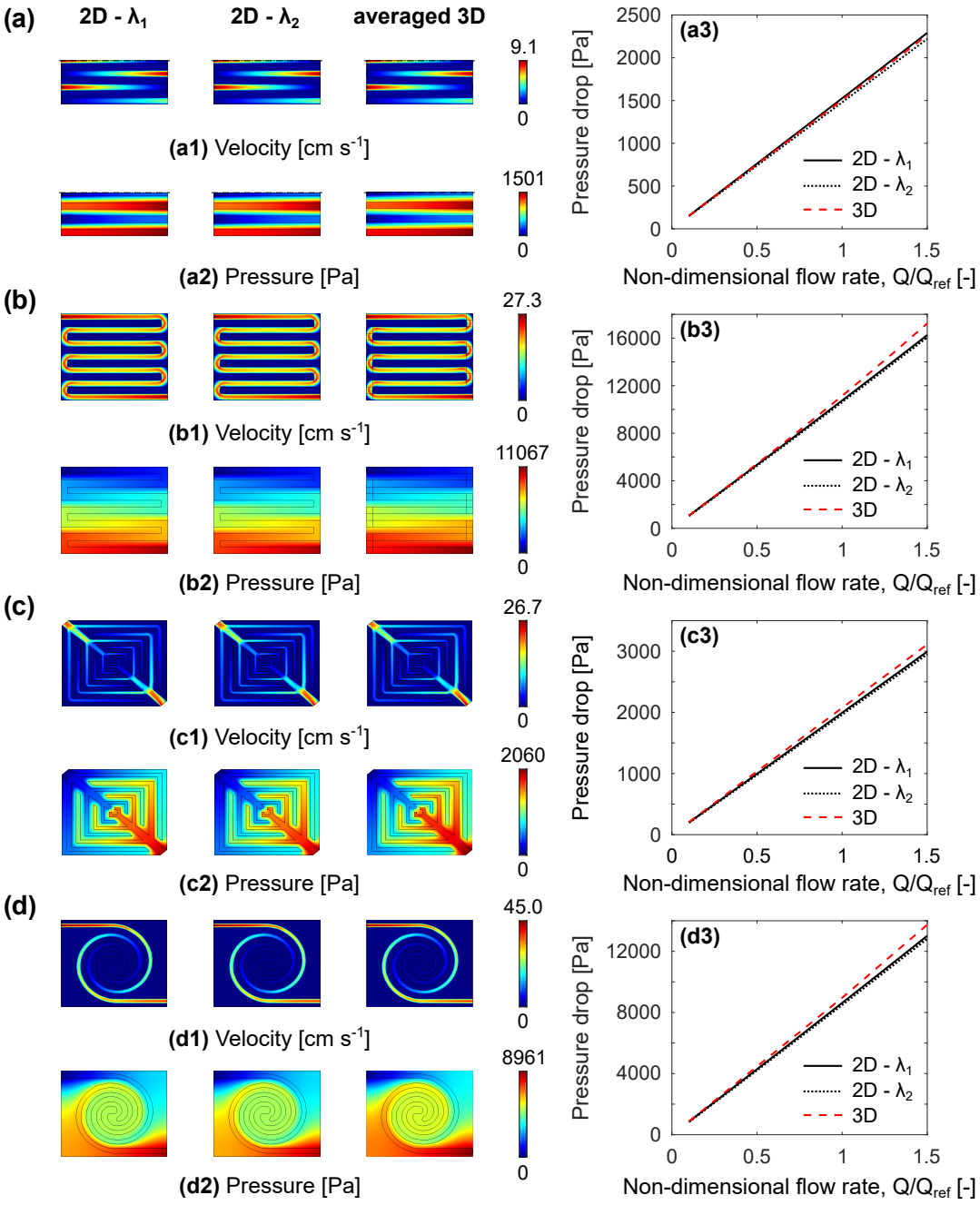

Figure 9: Comparison of fluid dynamic responses between 2D and 3D model with IDFF [27] (a), SFF [56] (b), and flow field geometries from [57] (c) and [54] (d) in velocity (1) and pressure (2) at Q_{ref} ($10\,\mathrm{mL\,min^{-1}}$), and pressure drop versus various flow rates from $1-15\,\mathrm{mL\,min^{-1}}$ (3). λ_1 and λ_2 refer to values estimated through Eq. (15) and Eq. (10), respectively.

d); for example, the discrepancy at $15\,\mathrm{mL\,min^{-1}}$ for SFF reaches $6.69\,\%$ using λ_2. This is caused by the channel bends, as discussed in Behrou et al. [28]. Fig. S24 of the Supporting Information presents the result from further investigations on such effect, taking SFF as an example. A new 3D pressure drop that eliminates the effects of channel bends ("3D - single channel" of Fig. S24a of the Supporting Information) is estimated by multiplying the single-channel pressure drop (Fig. S24b of the Supporting Information) by the number of channels. As shown in Fig. S24 of the Supporting Information, eliminating the bend effect significantly reduces the discrepancy at high flow rate, from $\approx 7\,\%$ to $< 2\,\%$. This effect can be averted by augmenting an additional quadratic Forchheimer drag term [36] , which changes with respect to the geometry [28] and will be the focus of future work. Additionally, the two different λ estimations give very close results of ca. $1 - 1.5\,\%$ throughout the entire flow rate range; therefore, we can directly use Eq. (10) for analyzing a new geometry.

4. Conclusions

In this work, we generate a depth-averaged, 2D fluid dynamic model for the electrode and flow field domains in a redox flow half cell. Comparing with the 3D simulations, we are able to capture the pressure discrepancies using a correction factor, λ, whose optimal value is evaluated across various flow field geometries. We find that λ is best described through the empirical relationships between the electrode thickness and the rib width, enabling model accuracy between the depth-averaged model and the 3D model of $< 5\%$. Furthermore, for structures with ill-defined channel widths, we propose an equivalent rib quantity, accounting for the total rib area and its entire wetted perimeter, including the inlet and outlet interfaces. Effectively a hydraulic diameter, this quantity enables good agreement between the depth-averaged and 3D fluid dynamic models of generic, hypothetical, and previously published flow field domains.

This depth-averaged model can enable high-throughput simulations of fluid dynamic behavior across various flow fields with minimal computational overhead. However, integration of the electrochemical process is needed to fully describe RFB cell performance, and will be the focus of follow-up studies. Importantly, this modeling approach affords a platform for diverse topological optimization procedures, leveraging the computational lightness to realize bottom-up flow field designs tuned for a particular electrochemical environment.

5. Acknowledgments

K.M.T., Y.-M.C., and F.R.B. are thankful for the financial support from the Joint Center for Energy Storage Research, an Energy Innovation Hub funded by the U.S. Department of Energy, Office of Science, Basic Energy (De-AC02-06CH11357). K.M.T. acknowledges additional funding from the U.S. National Science Foundation Graduate Research Fellowship (1122374). Any opinion, findings, and conclusions or recommendations expressed in this material are those of the authors and do not necessarily reflect the views of the National Science Foundation. A.F.-C. acknowledges funding from the Dutch Research Council (NWO) for the Veni Grant (17324). Z.C. thanks Politecnico di Torino for its support. R.B. acknowledges the University of California, San Diego for its support.

6. CRediT authorship contribution statement

Ziqiang Cheng: Conceptualization, Methodology, Validation, Formal analysis, Investigation, Data curation, Writing - original draft, Writing - review & editing, Visualization. **Kevin M. Tenny:** Conceptualization, Methodology, Validation, Formal analysis, Investigation, Writing - original draft, Writing - review & editing, Visualization. **Alberto Pizzolato:** Methodology, Resources, Writing - review & editing. **Antoni Forner-Cuenca:** Writing - review & editing, Supervision. **Vittorio Verda:** Resources. **Yet-Ming Chiang:** Resources. **Fikile R. Brushett:** Resources, Writing - review & editing, Supervision. **Reza Behrou:** Conceptualization, Methodology, Writing - original draft, Writing - review & editing, Supervision.

References

[1] Z. Yang, J. Zhang, M. C. W. Kintner-Meyer, X. Lu, D. Choi, J. P. Lemmon, J. Liu, Electrochemical Energy Storage for Green Grid, Chemical Reviews 111 (2011) 3577–3613. doi:10.1021/cr100290v.

[2] A. Z. Weber, M. M. Mench, J. P. Meyers, P. N. Ross, J. T. Gostick, Q. Liu, Redox flow batteries: A review, Journal of Applied Electrochemistry 41 (2011) 1137–1164. doi:10.1007/s10800-011-0348-2.

[3] P. Leung, X. Li, C. Ponce de León, L. Berlouis, C. T. J. Low, F. C. Walsh, Progress in redox flow batteries, remaining challenges and their applications in energy storage, RSC Advances 2 (2012) 10125. doi:10.1039/c2ra21342g.

[4] K. Lourenssen, J. Williams, F. Ahmadpour, R. Clemmer, S. Tasnim, Vanadium redox flow batteries: A comprehensive review, Journal of Energy Storage 25 (2019) 100844. doi:10.1016/j.est.2019.100844.

[5] M. Skyllas-Kazacos, M. H. Chakrabarti, S. A. Hajimolana, F. S. Mjalli, M. Saleem, Progress in Flow Battery Research and Development, Journal of The Electrochemical Society 158 (2011) R55. doi:10.1149/1.3599565.

[6] Y. Shi, C. Eze, B. Xiong, W. He, H. Zhang, T. M. Lim, A. Ukil, J. Zhao, Recent development of membrane for vanadium redox flow battery applications: A review, Applied Energy 238 (2019) 202–224. doi:10.1016/j.apenergy.2018.12.087.

[7] J. Balaji, M. G. Sethuraman, S.-H. Roh, H.-Y. Jung, Recent developments in sol-gel based polymer electrolyte membranes for vanadium redox flow batteries – A review, Polymer Testing 89 (2020) 106567. doi:10.1016/j.polymertesting.2020.106567.

[8] M. R. Gerhardt, A. A. Wong, M. J. Aziz, The Effect of Interdigitated Channel and Land Dimensions on Flow Cell Performance, Journal of The Electrochemical Society 165 (2018) A2625–A2643. doi:10.1149/2.0471811jes.

[9] Q. Xu, T. Zhao, P. Leung, Numerical investigations of flow field designs for vanadium redox flow batteries, Applied Energy 105 (2013) 47–56. doi:10.1016/j.apenergy.2012.12.041.

[10] R. M. Darling, M. L. Perry, The Influence of Electrode and Channel Configurations on Flow Battery Performance, Journal of The Electrochemical Society 161 (2014) A1381–A1387. doi:10.1149/2.0941409jes.

[11] B. K. Chakrabarti, E. Kalamaras, A. K. Singh, A. Bertei, J. Rubio-Garcia, V. Yufit, K. M. Tenny, B. Wu, F. Tariq, Y. S. Hajimolana, N. P. Brandon, C. T. J. Low, E. P. L. Roberts, Y.-M. Chiang, F. R. Brushett, Modelling of redox flow battery electrode processes at a range of length scales: A review, Sustainable Energy & Fuels 4 (2020) 5433–5468. doi:10.1039/D0SE00667J.

[12] Q. Zheng, X. Li, Y. Cheng, G. Ning, F. Xing, H. Zhang, Development and perspective in vanadium flow battery modeling, Applied Energy 132 (2014) 254–266. doi:10.1016/j.apenergy.2014.06.077.

[13] Q. Zheng, H. Zhang, F. Xing, X. Ma, X. Li, G. Ning, A three-dimensional model for thermal analysis in a vanadium flow battery, Applied Energy 113 (2014) 1675–1685. doi:10.1016/j.apenergy.2013.09.021.

[14] C. Yin, S. Guo, H. Fang, J. Liu, Y. Li, H. Tang, Numerical and experimental studies of stack shunt current for vanadium redox flow battery, Applied Energy 151 (2015) 237–248. doi:10.1016/j.apenergy.2015.04.080.

[15] M. Messaggi, P. Canzi, R. Mereu, A. Baricci, F. Inzoli, A. Casalegno, M. Zago, Analysis of flow field design on vanadium redox flow battery performance: Development of 3D computational fluid dynamic model and experimental validation, Applied Energy 228 (2018) 1057–1070. doi:10.1016/J.APENERGY.2018.06.148.

[16] C. Yin, Y. Gao, G. Xie, T. Li, H. Tang, Three dimensional multi-physical modeling study of interdigitated flow field in porous electrode for vanadium redox flow battery, Journal of Power Sources 438 (2019) 227023. doi:10.1016/j.jpowsour.2019.227023.

[17] J. Lee, J. Kim, H. Park, Numerical simulation of the power-based efficiency in vanadium redox flow battery with different serpentine channel size, International Journal of Hydrogen Energy 44 (2019) 29483–29492. doi:10.1016/j.ijhydene.2019.05.013.

[18] C. Yuan, F. Xing, Q. Zheng, H. Zhang, X. Li, X. Ma, Factor analysis of the uniformity of the transfer current density in vanadium flow battery by an improved three-dimensional transient model, Energy 194 (2020) 116839. doi:10.1016/j.energy.2019.116839.

[19] D. Zhang, A. Forner-Cuenca, O. O. Taiwo, V. Yufit, F. R. Brushett, N. P. Brandon, S. Gu, Q. Cai, Understanding the role of the porous electrode microstructure in redox flow battery performance using an experimentally validated 3D pore-scale lattice Boltzmann model, Journal of Power Sources 447 (2020) 227249. doi:10.1016/j.jpowsour.2019.227249.

[20] L. Chen, Y. He, W.-Q. Tao, P. Zelenay, R. Mukundan, Q. Kang, Pore-scale study of multiphase

reactive transport in fibrous electrodes of vanadium redox flow batteries, Electrochimica Acta 248 (2017) 425–439. doi:10.1016/j.electacta.2017.07.086.

[21] G. Qiu, A. S. Joshi, C. Dennison, K. Knehr, E. Kumbur, Y. Sun, 3-D pore-scale resolved model for coupled species/charge/fluid transport in a vanadium redox flow battery, Electrochimica Acta 64 (2012) 46–64. doi:10.1016/j.electacta.2011.12.065.

[22] Y. Chen, J. Bao, Z. Xu, P. Gao, L. Yan, S. Kim, W. Wang, A two-dimensional analytical unit cell model for redox flow battery evaluation and optimization, Journal of Power Sources 506 (2021) 230192. doi:10/gk76wz.

[23] D. A. Cogswell, M. Z. Bazant, Size-dependent phase morphologies in lifepo4 battery particles, Electrochemistry Communications 95 (2018) 33–37.

[24] D. Li, L. Song, C. Zhang, L. Yu, X. Xuan, A depth-averaged model for newtonian fluid flows in shallow microchannels, Physics of Fluids 33 (2021) 012002.

[25] H. Tian, M. A. Alkhadra, M. Z. Bazant, Theory of shock electrodialysis i: Water dissociation and electrosmotic vortices, Journal of Colloid and Interface Science 589 (2021) 605–615.

[26] A. K. Sharma, C. Y. Ling, E. Birgersson, M. Vynnycky, M. Han, Verified reduction of dimensionality for an all-vanadium redox flow battery model, Journal of Power Sources 279 (2015) 345–350. doi:10.1016/j.jpowsour.2015.01.019.

[27] Z. Cheng, K. M. Tenny, A. Pizzolato, A. Forner-Cuenca, V. Verda, Y.-M. Chiang, F. R. Brushett, R. Behrou, Data-driven electrode parameter identification for vanadium redox flow batteries through experimental and numerical methods, Applied Energy 279 (2020) 115530. doi:10.1016/j.apenergy.2020.115530.

[28] R. Behrou, A. Pizzolato, A. Forner-Cuenca, Topology optimization as a powerful tool to design advanced PEMFCs flow fields, International Journal of Heat and Mass Transfer 135 (2019) 72–92. doi:10.1016/j.ijheatmasstransfer.2019.01.050.

[29] K. Shiono, D. W. Knight, Turbulent open-channel flows with variable depth across the channel, Journal of Fluid Mechanics 222 (1991) 617–646. doi:10.1017/S0022112091001246.

[30] D. W. Knight, M. Omran, X. Tang, Modeling Depth-Averaged Velocity and Boundary Shear in Trapezoidal Channels with Secondary Flows, Journal of Hydraulic Engineering 133 (2007) 39–47. doi:10.1061/(ASCE)0733-9429(2007)133:1(39).

[31] Y. G. Lai, Two-Dimensional Depth-Averaged Flow Modeling with an Unstructured Hybrid Mesh, Journal of Hydraulic Engineering 136 (2010) 12–23. doi:10.1061/(ASCE)HY.1943-7900.0000134.

[32] D. L. George, R. M. Iverson, A depth-averaged debris-flow model that includes the effects of evolving dilatancy. II. Numerical predictions and experimental tests, Proceedings of the Royal Society A: Mathematical, Physical and Engineering Sciences 470 (2014) 20130820. doi:10.1098/rspa.2013.0820.

[33] X. Xia, Q. Liang, A new depth-averaged model for flow-like landslides over complex terrains with curvatures and steep slopes, Engineering Geology 234 (2018) 174–191. doi:10.1016/j.enggeo.2018.01.011.

[34] M. Ehrhardt, An Introduction to Fluid-Porous Interface Coupling, Coupled Fluid Flow in Energy, Biology and Environmental Research (2012) 3–12. doi:10.2174/978160805254711201010003.

[35] R. L. Panton, Incompressible Flow, fourth ed., Wiley, 2013. doi:10.1002/9781118713075.

[36] D. A. Nield, A. Bejan, Convection in Porous Media, 3rd ed ed., Springer, New York, 2006. doi:10.1007/978-3-319-49562-0.

[37] X. Ke, J. M. Prahl, J. I. D. Alexander, R. F. Savinell, Redox flow batteries with serpentine flow fields: Distributions of electrolyte flow reactant penetration into the porous carbon electrodes and effects on performance, Journal of Power Sources 384 (2018) 295–302. doi:10.1016/j.jpowsour.2018.03.001.

[38] X. Ke, J. M. Prahl, J. I. D. Alexander, J. S. Wainright, T. A. Zawodzinski, R. F. Savinell, Rechargeable redox flow batteries: Flow fields, stacks and design considerations, Chemical Society Reviews 47 (2018) 8721–8743. doi:10.1039/C8CS00072G.

[39] J. Casey, Curvature of Curves, in: J. Casey (Ed.), Exploring Curvature, Vieweg+Teubner Verlag, Wiesbaden, 1996, pp. 113–136. doi:10.1007/978-3-322-80274-3_10.

[40] D. Cheng, M. Tian, B. Wang, J. Zhang, J. Chen, X. Feng, Z. He, L. Dai, L. Wang, One-step activation of high-graphitization N-doped porous biomass carbon as advanced catalyst for vanadium redox flow battery, Journal of Colloid and Interface Science 572 (2020) 216–226. doi:10.1016/j.jcis.2020.03.069.

[41] T. Jyothi Latha, S. Jayanti, Ex-situ experimental studies on serpentine flow field design for redox flow battery systems, Journal of Power Sources 248 (2014) 140–146. doi:10.1016/j.jpowsour.2013.09.084.

[42] T. Jyothi Latha, S. Jayanti, Hydrodynamic analysis of flow fields for redox flow battery applications, Journal of Applied Electrochemistry 44 (2014) 995–1006. doi:10.1007/s10800-014-0720-0.

[43] Q. Xu, T. Zhao, C. Zhang, Performance of a vanadium redox flow battery with and without flow fields, Electrochimica Acta 142 (2014) 61–67. doi:10.1016/j.electacta.2014.07.059.

[44] J. Houser, J. Clement, A. Pezeshki, M. M. Mench, Influence of architecture and material properties on vanadium redox flow battery performance, Journal of Power Sources 302 (2016) 369–377. doi:10.1016/j.jpowsour.2015.09.095.

[45] S. Kumar, S. Jayanti, Effect of flow field on the performance of an all-vanadium redox flow battery, Journal of Power Sources 307 (2016) 782–787. doi:10.1016/j.jpowsour.2016.01.048.

[46] Y. Zeng, F. Li, F. Lu, X. Zhou, Y. Yuan, X. Cao, B. Xiang, A hierarchical interdigitated flow field design for scale-up of high-performance redox flow batteries, Applied Energy 238 (2019) 435–441. doi:10.1016/j.apenergy.2019.01.107.

[47] R. Gundlapalli, S. Jayanti, Effect of electrolyte convection velocity in the electrode on the performance of vanadium redox flow battery cells with serpentine flow fields, Journal of Energy Storage 30 (2020) 101516. doi:10.1016/j.est.2020.101516.

[48] P. Rao, S. Jayanti, Influence of electrode design parameters on the performance of vanadium redox flow battery cells at low temperatures, Journal of Power Sources 482 (2021) 228988. doi:10.1016/j.jpowsour.2020.228988.

[49] C. Yin, Y. Gao, S. Guo, H. Tang, A coupled three dimensional model of vanadium redox flow battery for flow field designs, Energy 74 (2014) 886–895. doi:10.1016/j.energy.2014.07.066.

[50] I. The MathWorks, Curve Fitting Toolbox, Natick, Massachusetts, United State, 2020. URL: https://www.mathworks.com/products/curvefitting.html.

[51] M. Al-Yasiri, J. Park, Study on Channel Geometry of All-Vanadium Redox Flow Batteries, Journal of The Electrochemical Society 164 (2017) A1970. doi:10.1149/2.0861709jes.

[52] S. Maurya, P. T. Nguyen, Y. S. Kim, Q. Kang, R. Mukundan, Effect of flow field geometry on operating current density, capacity and performance of vanadium redox flow battery, Journal of Power Sources 404 (2018) 20–27. doi:10.1016/j.jpowsour.2018.09.093.

[53] A. Forner-Cuenca, E. E. Penn, A. M. Oliveira, F. R. Brushett, Exploring the Role of Electrode Microstructure on the Performance of Non-Aqueous Redox Flow Batteries, Journal of The Electrochemical Society 166 (2019) A2230–A2241. doi:10.1149/2.0611910jes.

[54] B. Ibrahimoglu, M. Z. Yilmazoglu, S. Celenk, Investigation of Spiral Flow-Field Design on the Performance of a PEM Fuel Cell, Fuel Cells 17 (2017) 786–793. doi:10.1002/fuce.201700076.

[55] COMSOL Multiphysics v. 5.3a, COMSOL AB, Stockholm, Sweden, 2017.

[56] J. D. Milshtein, K. M. Tenny, J. L. Barton, J. Drake, R. M. Darling, F. R. Brushett, Quantifying Mass Transfer Rates in Redox Flow Batteries, Journal of The Electrochemical Society 164 (2017) E3265. doi:10.1149/2.0201711jes.

[57] A. Arvay, J. French, Modeling and Simulation of Biologically Inspired Flow Field Designs for Proton Exchange Membrane Fuel Cells, The Open Electrochemistry Journal (2015) 9.